Image Enhancement by Linear Spatial Deconvolution: Recent Developments

Harry L. Graber[1,2], Yong Xu[1,2], Yaling Pei[1], and Randall L. Barbour[1,2]

[1]*NIRx Medical Technologies LLC, 15 Cherry Lane, Glen Head, NY 11545*

[2]*SUNY Downstate Medical Center, 450 Clarkson Ave., Brooklyn, NY 11203*

Introduction

Diffuse optical tomography (DOT) is a functional imaging modality capable of studying blood flow in normal and pathological tissues in real time. DOT employs harmless near infrared radiation to obtain measurements of absorption and scattering coefficients (μ_a and μ'_s) within tissue, which can be used to extract images of physiological parameters such as hemoglobin concentrations. The advantages of DOT, when compared to PET imaging or fMRI, include its low cost, superior temporal resolution, and fewer physical constraints on the subject. Potential drawbacks to DOT include its low spatial resolution and, consequently, lower quality images. Most strategies for improving image quality incorporate computation-intensive algorithms, which eliminate the possibility of studying tissue dynamics in a physiologically relevant time frame.

In an effort to improve image quality, a spatial deconvolution algorithm based on temporal encoding of spatial information was developed. This algorithm was shown to significantly improve qualitative and quantitative image accuracy, with a computational effort far lower than that required for recursive iterative reconstruction techniques [1]. Furthermore, it was shown that the tradeoff between enhancement of spatial resolution and degradation of temporal accuracy can be contained within acceptable bounds [2]. Subsequent refinements of the deconvolution algorithm are capable of performing equally well for 3-D imaging problems [3] and in restricted-view cases [4]. Previous characterizations of this approach were constrained by the use of a homogeneous background, and by the modeling of only temporally varying μ_a in the inclusions. To explore our image enhancement scheme systematically, we have investigated the effect of target medium complexity on the fidelity of the method and the method's ability to improve the quality of recovered images of the diffusion coefficient D ($\sim 1/\mu'_s$). Most recently, we conducted pilot solid-state dynamic phantom studies for validating the linear spatial deconvolution algorithm.

Influence of Background Medium Heterogeneity

The starting point for the geometrical model used was a 3D T1-weighted structural MRI image of the human head. As shown in Figure 1, six principal tissue types—scalp, muscle, skull, cerebrospinal fluid (CSF), gray matter, and white matter—were identified within the selected area. The corresponding finite element model and the source/detector configuration are depicted in Figure 2.

All surface detector data and internal photon intensities were obtained by performing finite element method (FEM) computations to numerically solve the diffusion equation with Robin boundary conditions [5]. Each forward-problem computation was performed four times, once for each of the four values of μ_a assigned to the CSF (Table 1).

Sinusoidal time-varying absorption coefficients in the inclusion volume and the grey matter of the model tissue compartments were used to evaluate the method's ability to recover dynamic information. In addition, images were reconstructed from data that were either noise-free or contaminated with white Gaussian additive noise (see Fig. 6). To assess the extent to which the effects of noise are reversible, elementary temporal and spatial low-pass filtering techniques were applied after the reconstruction and deconvolution steps [2].

Deconvolution operators and detector-readings time series were computed for four combinations of time-averaged optical parameters (Table 1). To examine the sensitivity of the image enhancement algorithm to a spatially complex mismatch between the optical parameters of the filter-generating and target media, every deconvolution operator was applied to the images reconstructed from each medium's detector data. Spatial and temporal correlations (SC and TC, respectively) were computed between the true properties of each target medium and all corresponding image time series.

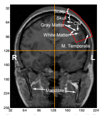

Figure 1. Coronal section of a 3D T1-weighted structural MRI of the human head, which was the starting point for the target medium used in simulation studies. The section shown intersects the pre-motor and primary motor cortices.

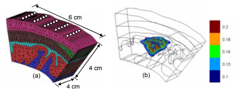

Figure 2. (a) Exterior view of the 3D model geometry generated from the MRI section shown in Fig. 1; source and detector positions also are indicated as small white circles. (b) Interior view of the 3D model from Fig. 2(a), revealing the inclusion embedded in the gray-matter zone.

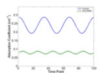

Figure 3. Plots of μ_a vs. time, in the inclusion and gray-matter compartments of the 3D tissue model of Fig. 2(b),(c).

	CSF		Inclusion		Others	
	μ_s (cm^{-1})	μ_a (cm^{-1})	μ_s (cm^{-1})	μ_a (cm^{-1})	μ_s (cm^{-1})	μ_a (cm^{-1})
Case1	10.0	0.080				
Case2	5.0	0.040		0.24		
Case3	1.0	0.010				
Case4	0.5	0.005	10.0		10.0	0.08
Filter1	10.0	0.080				
Filter2	5.0	0.040		0.08		
Filter3	1.0	0.010				
Filter4	0.5	0.005				

Table 1. Optical coefficient values (for tissue types with dynamic μ_a, tabulated number is the temporal mean) assigned to the different tissue compartments of the MRI-based 3D geometry, for all target (Case1-4) and reference (Filter1-4) media that were modeled.

Spatially convolved images are shown in Fig. 4(a),(c); the Fig. 4(a) result, Case1/Filter2, is computed using a weight function that under-estimates the CSF optical coefficients, while the Case3/Filter2 image [Fig. 4(c)] is obtained when weight functions are used that over-estimate the CSF optical coefficients. The noteworthy features of Figs. 4(a),(c) are that: they are qualitatively very similar; there is substantial depth location error, with the recovered μ_a perturbation apparently located within the skull; the size of the inclusion is over-estimated in all cases; the magnitude of the μ_a perturbation is under-estimated in all cases.

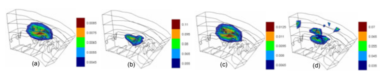

Figure 4. Volume rendering of the Fig. 2(b) target medium. (a) Case1 detector data, Filter2 reference medium (see Table 1), before deconvolution. (b) Case1 detector data, Filter2 reference medium, after deconvolution. (c) Case3 detector data, Filter2 reference medium (see Table 1), before deconvolution. (d) Case3 detector data, Filter2 reference medium, after deconvolution. In each sub-figure, the range of μ_a values plotted runs from $\mu_a^{max}/2$ to μ_a^{max}.

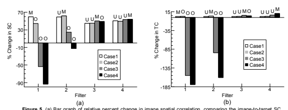

Figure 5. (a) Bar graph of relative percent change in image spatial correlation, comparing the image-to-target SC after and before spatial deconvolution, for all 16 Case/Filter pairings. (b) Bar graph of the corresponding relative percent changes in image temporal correlation. Annotations above bars indicate whether the reference-medium CSF optical coefficients match ('M'), over-estimate ('O') or under-estimate ('U') those of the target medium

Even though qualitative image accuracy is more variable after spatial deconvolution than before, the result obtained for the Case1/Filter2 pairing after deconvolution [Fig. 4(b); compare with Fig. 4(a)] is superior in depth location, inclusion size, and quantitative perturbation magnitude. In stark contrast, when the direction of the mismatch is reversed and the CSF optical coefficients are over-estimated [Fig. 4(d)], the high-absorption region of the deconvolved image splits into two parts: one at the correct location and the other consisting of superficial artifacts. Increasing the magnitude of the mismatch leads to a completely erroneous result (not shown) that consists almost exclusively of the superficial artifacts. Comparison of imaging results for all 16 Case/Filter pairings and all 100 time frames show that the type of trend seen in Fig. 4 turns up consistently.

The effect of deconvolution on the target image was quantified by computing the percent differences in the SC and TC before and after the procedure, for all 16 Case/Filter pairings [Figure 5(a) (spatial) and 5(b) (temporal)]. The white bars in Figure 5 represent data for the Case1 medium, where the CSF optical coefficients are never over-estimated, while the black bars include data for the Case4 medium, where CSF optical coefficients are never under-estimated. It can be seen that deconvolution for the Case1 medium always brings about an increase in SC and TC, while for the Case4 medium, the effect of deconvolution ranges from significant degradation of image quality to substantial improvement. Results for the other Cases are in between those for the preceding two.

Figure 6 shows the percent changes in SC [Fig. 6(a)] and TC [Fig. 6(b)], for all four Case*N*/Filter3 pairings and all three noise levels. As in Fig. 5, positive(negative) values indicate that the correlation is higher(lower) after deconvolution than before. By inspection, it can be observed that at the lowest noise level typical of data collected in DOT brain measurements: 1) the SC invariably increases upon spatial deconvolution; 2) the loss of TC associated with deconvolution can be minimized by using sLPF and tLPF in combination.

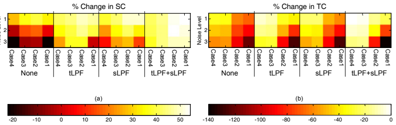

Figure 6. (a) Colormap of relative percent change in image spatial correlation, comparing the image-vs.-target SC before and after spatial deconvolution, for the four Case*N*/Filter3 pairings, three noise levels, and four varieties of noise suppression. (b) Colormap of the corresponding relative percent changes in image temporal correlation. We used a noise model in which, for each source-detector channel, the standard deviation of the noise distribution is a pre-selected percentage of the noise-free detector reading and grows as the fourth power of the distance between source and detector [5]. The minimal noise level (source and detector co-located) was 1, 2 or 3%, while the maximal noise level was, 10, 20 or 30%, respectively.

Recovery of Diffusion Coefficient Distributions

All of the simulations reported in this section used circular, 4-cm radius, 2D media. The modeled heterogeneities consisted of either one or two circular inclusions wherein D was approximately half that of the background region (i.e. μ'_s of the inclusion is approximately twice that of the background).

Two types of two-inclusion studies were performed, and in every case the inclusion diameter was fixed at 0.6 cm, with one centered at (x_c,y_c) and the other at (-x_c,y_c). For the first study, y_c was fixed at 0 and x_c was adjusted, in 0.1-cm increments, from a minimum of 0.3 cm (i.e., inclusions have a point of contact) to a maximum of 1.0 cm. For the second, x_c was fixed at 0.5 cm and y_c was adjusted, in 0.2-cm increments, from a minimum of 0.2 cm to a maximum of 3.0 cm. The particular case illustrated in Fig. 7 is $D(x,y)$ for inclusions centered at ($\pm$1,0).

In every simulation, the absorption coefficient was fixed at μ_a = 0.06 cm^{-1} throughout the medium, while the background scattering coefficient was $\mu'_{s,\mathrm{bkgr}}$ = 10 cm^{-1}, which, according to the relation $D = 1/[3(\mu'_s + \mu_a)]$, corresponds to a background diffusion coefficient of D_{bkgr} = 0.0331 cm. Within the inclusions, the time-averaged scattering coefficients were $\langle\mu'_{s,\mathrm{incl}}\rangle$ = 20 cm^{-1} for all one-inclusion and all noise-free two-inclusion computations, and $\langle\mu'_{s,\mathrm{incl}}\rangle$ = 30 cm^{-1} for the two-inclusion simulations with noise added to the detector data. Dynamic scattering was modeled through the relation $\mu'_{s,\mathrm{incl}}(t) = \langle\mu'_{s,\mathrm{incl}}\rangle[1 + 0.2\sin(2\pi\cdot f\cdot t)]$, with f = 0.1 Hz and t = 0.5, 1, ..., 49.5, 50 s. Thus D_{incl} ranges from 0.0139 to 0.0208 cm (0.00924-0.0139 cm for the noise-added two-inclusion case) with a mean value of 0.0170 (0.0113) cm.

All forward-problem and inverse-problem computations were carried out in the manner specified in Ref. 5. Reconstructed images [e.g., Fig. 9(a),(e)] were post-processed by applying the spatial deconvolution algorithm that was the subject of Refs. 1-4. The key distinction between these studies and the previous ones is that here μ'_s, rather than μ_a, was modulated in each reference-medium pixel. All modeled $\mu'_s(x,y)$ states were converted to the corresponding spatial distributions of D, and the deconvolution operator was generated by comparing the latter to the recovered D images, as explained in Refs. 1-4. To examine the effect of random error on the accuracy of recovered images, computations were conducted three times, with noise-free detector data used in the first instance, and with data to which Gaussian white noise was added in the remainder. The noise levels were 1% and 2%, where the noise level ε_k for the k^{th} S-D channel is defined as $\varepsilon_k = 100 s_k/m_{0k}$, where s_k is the standard deviation of the k^{th}-channel noise distribution, and m_{0k} is the time-averaged noise-free detector reading.

Recovered images were subsequently treated with a noise-suppression scheme consisting of a combination of temporal low-pass filtering (tLPF) and spatial "pillbox" filtering (sLPF) [2]. Comparisons between the target medium and reconstructed images, including the spatial and temporal correlation coefficients (SC and TC, respectively), and spatial and temporal root mean squared error (sRMSE and tRMSE, respectively), are used here as global indices of spatial and temporal accuracy of recovered images [5]. Several "local" measures of image quality also were computed (see Fig. 10). The parameters from which the latter were computed are defined in Figure 8.

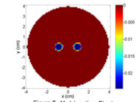

Figure 7. Model medium $D(x,y)$

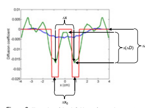

Figure 8. Illustration of the definitions of several parameters used in calculating indices of image accuracy.

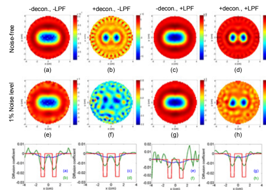

Figure 9. Recovered images of the target medium depicted in Fig. 7. (a)-(d) Detector data are noise free; (e)-(h) detector data noise level is 1%. (a),(e) –decon, -LPF images; (b),(f) +decon, -LPF images; (c),(g) –decon, +LPF images; (d),(h) +decon, +LPF images. (i)-(l) 1D sections through images in (a)-(h), along the y = 0 diameter.

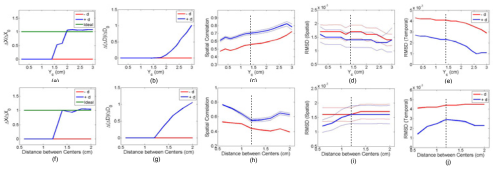

Figure 10. Summary indices of qualitative and quantitative image accuracy

Representative images and 1D sections for a two-inclusion target medium, time frame and inclusion location [(x_c, y_c) = (±0.9, 0)], are shown in Figure 9. Qualitatively, the trends seen in these results agree with those previously reported for target media containing μ_a perturbations [4]. Overall, the results demonstrate that the spatial deconvolution yields significantly improved images, in terms of spatial resolving power and quantitative accuracy. However, deconvolution tends to amplify any background artifacts, whether they originate from systematic factors or from random errors. Consequently, when the detector data are noisy, the inclusions continue to be recovered with fair accuracy, but the amplitudes of noise artifacts can become comparable to those of the inclusions. By using the tLPF and sLPF in combination [2], the background artifacts are substantially reduced, at the cost of some reduction in quantitative accuracy.

Various scalar indices of image accuracy are plotted in Figure 10. Results for the variable-y_c study are in Fig. 10(a)-(e), and those for a complementary variable-x_c (y_c fixed at 0) are in Fig. 10(f)-(j). Neither of the resolving-power indices [Fig. 10(a),(b),(f),(g)] rises above zero for the spatially convolved images. For the deconvolved images, partial resolution is seen when y_c > 1.4 cm in Fig. 10(a). It can be observed from the other quantities plotted in Fig. 10 (the SC, sRMSE and tRMSE) that after deconvolution, the SC is significantly higher, while the sRMSE and tRMSE are substantially lower, than before deconvolution. The vertical dashed lines in Fig. 10 are located at the values of y_c or x_c at which the inclusions begin to be resolved.

Preliminary Results of Dynamic Phantom Studies

Recently, we have developed a dynamic calibrating phantom system [6] that employs electrochromic (EC) technology as a basis for electronically modulating the optical properties of an inclusion within a scattering medium. Fig. 11(a) shows the tissue-like brain-shaped phantom, with an EC cell embedded up to a depth of ~2cm below the surface of the plastic skull. Figure 11(b) illustrates the finite element model used in the image reconstruction, as well as the location of EC cell embedded in gray matter. The variation of the optical properties of the EC cell, which mimics a blood volume change, is plotted in Fig. 11(c). In our dynamic phantom experiment, a 5×5 array of illumination-detection fibers, located at the surface of the skull, is used as illustrated in Fig. 11(a). The experimental data sets are measured by our DYNOT Imager.

Figure 12 demonstrates recovered results obtained by using our linear spatial deconvolution method. Shown in panels (a) and (b) of Figure 12 are GLM coefficient maps wherein the EC cell input function (see Fig. 11c) was used as the modeled response. Inspection reveals that in the absence of deconvolution, the inclusion is localized in the more superficial regions of the tissue, and not where it is truly located (i.e. motor cortex) – a result that resembles findings seen with the MR simulated brain (Figure 4). A notably improved result is seen in Panel (b), where the recovered location overlaps with estimates of the true location as judged by CT imaging. It can also be observed that the recovered GLM coefficients following deconvolution are more than ten-fold greater than those seen in the unprocessed image. The last column of Figure 12 shows a comparison at the pixel level, where the blue tracing is within the region of maximal GLM values and the green is outside. Notice the correlation evident between the two pixels in the unprocessed image [Panel (a)], which we take as evidence of spatial blurring, and its absence following application of the deconvolution operator.

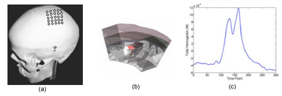

Figure 11. (a) Head-shaped phantom and source/detector configuration; (b) Finite element model and location of embedded EC cell; (c) Modeled dynamic response of the EC cell.

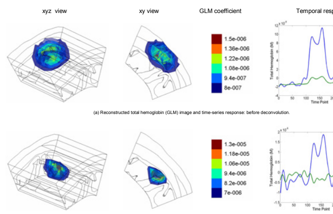

(a) Reconstructed total hemoglobin (GLM) image and time-series response: before deconvolution.

(b) Reconstructed total hemoglobin (GLM) image and time-series response: after deconvolution.

Figure 12: Brain phantom with skull: Total hemoglobin images and pixel temporal responses.

Conclusions

1. The image-enhancing effects of spatial deconvolution are not degraded by static or dynamic background heterogeneity, irregular external boundaries, or irregular, non-convex, interior region interfaces.
2. Performance is not degraded by levels of noise typically associated with DOT brain imaging studies.
3. A large mismatch between the background optical coefficients of the target and reference media may yield highly artifactual images, especially if the absorption and scattering of the reference medium are over-estimated. Qualitatively similar artifacts can occur if the measurement data are excessively noisy.
4. The linear deconvolution algorithm have been extended to enhance the accuracy of DOT images to include spatial maps of the scattering coefficient. The types and magnitudes of image-enhancing effects obtained here are similar to those found in the previous studies on μ_a perturbations.
5. The linear spatial deconvolution method has been experimentally validated by a dynamic head phantom.

In summary, we have developed a highly efficient linear spatial deconvolution technique that is capable of improving image quality of linear reconstructions in a broad array of tested media containing multiple inclusions, with either absorption or scattering contrast, capable of simple or complex dynamic behaviors. We have also shown that the technique is equally effective in the case of media having complex backgrounds and have experimentally validated this finding in a dynamic phantom modeling a sudden change in blood volume. A corollary to these findings is the inescapable conclusion that much of the image blurring seen in first-order solutions to the DOT inverse problem is not due to neglect of higher order, nonlinear, effects. The effects present are a linear convolution, seemingly brought about by the mathematical operations inherent to linear algebraic techniques.

References

1. R.L. Barbour, H.L. Graber, Y. Xu, Y. Pei, and R. Aronson, "Strategies for imaging diffusing media," *Transport Theory and Statistical Physics* **33**: 361-371 (2004).
2. Y. Xu, Y. Pei, H.L. Graber, and R.L. Barbour, "Image quality improvement via spatial deconvolution in optical tomography: Time-series imaging," *J. Biomedical Optics* **10**: 051701 (2005).
3. H.L. Graber, Y. Xu, Y. Pei, and R.L. Barbour, "Spatial deconvolution technique to improve the accuracy of reconstructed three-dimensional diffuse optical tomographic images," *Applied Optics* **44**: 941-953 (2005).
4. Y. Xu, H.L. Graber, Y. Pei, and R.L. Barbour, "Improved accuracy of reconstructed diffuse optical tomographic images by means of spatial deconvolution: two-dimensional quantitative characterization," *Applied Optics* **44**: 2115-2139 (2005).
5. Y. Pei, H.L. Graber, and R.L. Barbour, "Influence of systematic errors in reference states on image quality and on stability of derived information for DC optical imaging," *Applied Optics* **40**: 5755–5769 (2001).
6. R.L. Barbour, H.L. Graber, Y. Xu, Y. Pei, R. Ansari, and M. B. Levin, "An experimental calibrating system for functional DOT imaging," This conference, Poster [76], 4:30-6:30 pm on Monday.

Acknowledgment

This research was support in part by the National Institutes of Health (NIH) under Grants R21-HL67387, R21-DK63692, R41-CA96102 and R43-NS49734, and by the US Army under Grant DAMD017-03-C-0018.